AN ABSTRACT OF THE THESIS OF

Fanghui Ren for the degree of Master of Science in Electrical and Computer Engineering presented on June 14, 2012.

Title: Radiation Tolerance of Magnetic Tunnel Junctions with MgO Barriers .

Abstract approved:

____

Albrecht Jander

In the next decade, technology trends—smaller dimension, lower voltage, higher operating frequency—introduce new technical considerations and challenges for radiation effects in integrated circuits. Semiconductor based circuits and traditional dynamic random-access memories will malfunction when exposed to extreme environments, such as space and nuclear reactor. The mechanisms for radiation effect are mainly attributed to the radiation-induced charging of the oxide in a CMOS device. Spintronics is an emerging area of nanoscale electronics involving the detection and manipulation of electron spin. The magnetic tunnel junctions (MTJs), based on the intrinsic spin of the electron, can be used as the storage elements in non-volatile magnetoresistive random-access memories (MRAMs). In this effort, we study radiation tolerance of MTJs by exposing the devices in gamma and neutron radiation environment. Theoretical model for the radiation-induced defects is analyzed in this work. Experiments of the MgO-based MTJs under the conditions of pre- and post-radiation are concluded. MTJs were irradiated with gamma ray to a total dose of 10 Mrad. During the neutron irradiation, total epithermal neutron fluence up to $2.9\times10^{15}/\text{cm}^2$ was obtained. The experimental results show that neither the electrical nor the magnetic properties of MTJs are affected by the radiation.

Radiation Tolerance of Magnetic Tunnel Junctions with MgO Barriers

by
Fanghui Ren

A THESIS

submitted to

Oregon State University

in partial fulfillment of
the requirements for the
degree of

Master of Science

Presented June 14, 2012
Commencement June 2013

Master of Science thesis of Fanghui Ren presented on June 14, 2012

APPROVED:

Major Professor, representing Electrical and Computer Engineering

Director of the School of Electrical Engineering and Computer Science

Dean of the Graduate School

I understand that my thesis will become part of the permanent collection of Oregon State University libraries. My signature below authorizes release of my thesis to any reader upon request.

Fanghui Ren, Author

ACKNOWLEDGEMENTS

First, I would like to express my gratitude and respect to my major advisor, Prof. Albrecht Jander. I thank him for giving me the chance to be his student and supporting me to get this master degree. In the past two years, he has been teaching me how to be a reasonable researcher. I would also like to thank him for giving me his continual advice and wisdom throughout this project. I also want to express my appreciation to Prof. Pallavi Dhagat. I thank her for her persistent encouragement and help throughout all my master years.

I would also like to thank members in Magnetics group for various help, and I am honored of working with them: Weiyang Li, Han Song, Ben Buford, Pratim Chowdhury, Jonah Gross, Aaron Cochran, Sam Mulley, Tim Niedermeyer. I also want to thank my friends, Chao Ma, Fang Yuan, Jiao Cheng, Ce Cheng, Yonglei Zheng and others who have been spending the excellent time with me.

Finally, I would like thank my family members for years of support and encouragement.

TABLE OF CONTENTS

Page

1 Introduction 1

1.1 Motivation of the Project 1

1.2 Thesis Organization 3

2 Magnetic Tunnel Junction 5

2.1 Spin-valve Structure 5

2.2 Magnetoresistance 6

2.2.1 AMR and GMR 6

2.2.2 TMR and Jullière’s Model 8

2.3 Important Features 14

2.3.1 Voltage Dependence 14

2.3.2 Temperature Dependence 17

2.4 Conclusion 19

3 Radiation Effects 21

3.1 Basic Radiation Mechanisms 21

3.2 Radiation Effects in CMOS Devices 23

3.2.1 Photon- and Neutron-induced Effects 23

3.2.2 Device Scaling and Radiation Hardness 28

3.3 Radiation-induced Disorder in Magnetic Tunnel Junction 30

3.4 Conclusion 33

4 Experimental Results 34

4.1 Device Structure 34

TABLE OF CONTENTS(Continued)

Page

4.2 Measurement Techniques..35

4.3 Results and Analysis 37

5 Conclusion and Future Work 42

Bibliography 44

LIST OF FIGURES

Figures Page

Figure 2.1 A schematic diagram of a spin valve. (a)When the magnetic layers are antiparallel, the resistance is higher than when they are in parallel. (b)The hysterics loop of the MTJ. 5

Figure 2.2 A schematic diagram of a magnetoresistive random access memory. 6

Figure 2.3 GMR effects in a Fe/Cr/Fe multilayer structure, reprinted with permission from [Grünberg, 1988]. Left panel Fe/Cr/Fe shows the sandwich structure. Right panel shows (a) and (b) the hysteresis curves of the device (c) and (d) the resistance as a function of the applied field. In (a) and (c), the field is along easy axis, while in (b) and (d) the field is along the hard axis. 7

Figure 2.4 The first observation of reproducible large TMR in a CoFe/Al_2O_3/Co MTJ at room temperature, reprinted with permission from [Moodera, 1995]. 9

Figure 2.5 A schematic diagram of spin density of states in a non-magnetic material and ferromagnetic material. 10

Figure 2.6 Left panel shows An MTJ characterized by parallel or antiparallel magnetization of the left and right ferromagnetic layers. Middle panels shows the schematic representation of transitions between exchange-split spin bands in the ferromagnetic layers. The equivalent circuit diagram is shown on the right panel. 11

Figure 2.7 Coherent spin dependent tunneling in MgO barrier, reprinted with permission from [Yuasa, 2008]. Left panel shows there is only Δ_1 electrons with one spin polarization at the Fermi energy. Middle panel shows the coherent tunneling of electrons with symmetries. Right panel indicates the Δ_1 electrons have the lowest decay rate in the barrier. 13

Figure 2.8 Left panel shows a wave-function of a single electron, which is exponentially attenuated within the barrier. Right panel shows the energy diagram of a metal/insulator/metal tunnel junction. 14

Figure 2.9 The Matlab plot of I-V curve for a tunneling structure FeCo/MgO/FeCo with an effective junction area of 5 μm^2, an effective barrier height 0.9 eV, and a barrier thickness of 12Å. 15

Figure 2.10 (a) Both antiparallel parallel resistances decrease with increasing the voltage. (b) The overall TMR decreases with increasing the voltage. 16

LIST OF FIGURES (Continued)

Figure Page

Figure 2.11 The temperature dependence of TMR as a function of biased voltage, reprinted with permission from [Yuan, 2006]. 18

Figure 2.12 (a) Both antiparallel parallel resistances decrease with increasing the temperature. (b) The overall TMR decrease with increasing the temperature. 18

Figure 3.1 The illustration of a Frenkel pair in atomic lattice 22

Figure 3.2 The fraction of holes that escape initial recombination for x rays, low energy protons, gamma rays, and alpha particles, reprinted with permission from [Schwank, 2008] 24

Figure 3.3 Schematic energy band diagram for MOS structure, indicating physical processes underlying radiation response 25

Figure 3.4 Illustration of transistor in normal operation and post irradiation................... 26

Figure 3.5 Illustration of the effect of fixed oxide trapped charge on n- and p-MOS devices.. 26

Figure 4.1 The cross section of an MTJ stack 34

Figure 4.2 The experimental setup for Gamma radiation test 36

Figure 4.3 The neutron spectrum in CLICIT 37

Figure 4.4 The experimental setup for neutron radiation test... 37

Figure 4.5 Characteristics of a single MTJ before and after exposure to the gamma radiation. (a) The hysteresis loop representing the two resistance states. (b) The voltage bias dependence of the low resistance (R_{low}) state and high resistance (R_{high}) state. 38

Figure 4.6 Hc and TMR of a series of MTJs before and after exposure to the gamma radiation. (a) Characteristics of the experimental group. (b) Characteristics of the control group, which was not irradiated.. 39

Figure 4.7 Hc and TMR of a series of MTJs before and after exposure to the neutron radiation. (a) Characteristics of the experimental group. (b) Characteristics of the control group, which was not irradiated.. 40

LIST OF TABLES

Tables Page

Table 1 Typical K_g for different semiconductor materials. 25

Table 2 Failure level for typical ICs 30

Table 3 Spin Polarization and TMR in ideal MTJs and disorder-in-barrier MTJs........... 31

Radiation Tolerance of Magnetic Tunnel Junctions with MgO barriers

1 Introduction

1.1 Motivation of the Project

In order to satisfy the increasing demand for higher density and lower power, as the dimensions and operating voltages of electronic devices are reduced, their sensitivity to radiation increases dramatically. Semiconductor based circuits and traditional dynamic random-access memories will malfunction or be damaged when exposed to extreme environments, such as space [Dodd, 2010]. Approximately 89% of cosmic rays are protons, and 10% are alpha particles (helium nuclei), and 1% are heavy ions. Environments with these particles, as well as the secondary particles generated from the primary interaction, e.g. electrons, photons, neutrons, create special design challenges for electronic components and systems.

The Van Allen radiation belt, which is located in the inner region of the Earth's magnetosphere, poses a hazard to integrated circuits of the satellites. A combination of protons and electrons mainly forms the inner and outer belts. The flux of the electrons has altitude dependence, which ranges from 1.2×10^6/cm^{2}sec up to 9.4×10^9/cm^{2}sec, with energies greater than 500 keV at the magnetic equator. The kinetic energies of protons range from about 100 keV to over 400 MeV. For low energy protons with average energy of 100 keV, the proton flux could exceed 3×10^8 /cm^{2}sec, while a 100 MeV proton will have an approximate flux of 2×10^4 /cm^{2}sec [Hess, 1962]. The belts can cause damage to the satellites, which must protect their sensitive components with adequate shielding. Light metal, such as Aluminum is suitable for shielding because its low atomic weight introduces less Bremsstrahlung radiation compared with heavy metal. In conclusion, electronic devices on the satellites must be radiation hardened to operate reliably. Other radiation damage source, such as nuclear reactor, which is based on nuclear fission, produces gamma radiation and neutron radiation, can affect sensing and control circuits. Nuclear explosions, such as nuclear weapons, pose concerns for military electronics.

A sea level cosmic ray could cause a single event upset (SEU) in electronics, which describes the flipping of the state of memory cells. The terrestrial neutrons can be a major source of single event upsets (SEUs) in electronics devices. The measurement of the energy spectrum for the sea level neutrons from Gordon shows a broad range of neutrons, which ranges from meV to GeV [Gordon, 2004]. The analytical mode also indicates that, from the spectrum, the neutron flux ranges from 10^{-4} to 10^{-3}/cm^{2}sec, could exceed 10^{-3} at several peak energies. High energy neutrons have become increasingly significant for current technologies due to aggressive scaling of the critical dimensions and reduced voltages. Thermal neutrons with energy lower than 1 eV, have been shown to be an important source for SEUs in CMOS technologies with borophosphosilicate glass (BPSG) containing boron, due to the large thermal-neutron cross section of ^{10}B.

Basic radiation source can be grouped into two types, ionizing radiation and non-ionizing radiation. Ionization occurs when an electron is knocked out from an electron shell by the interaction with high energy photons and charged particles, such as gamma, alpha, beta, and X-ray. Neutrons do not directly ionize atoms, however, the collision and reaction with the atomic nuclei of many elements creates unstable isotopes and inducing radioactivity in a previously non-radioactive material. Other non-ionizing radiation includes thermal radiation and electromagnetic radiation, e.g., radio waves, microwaves, infrared.

Discovered in 1980s, a technology has emerged called spintronics, which exploits intrinsic spin of the electron instead of charge degrees of freedom. Spintronics provides opportunities for novel solid state devices combining traditional semiconductor devices with spin-dependent transport properties. Compared with traditional semiconductor technologies, the spin-based devices have several advantages, such as nonvolatility, low power consumption, high switching speed, and large integration densities [Wolf, 2001]. A magnetic tunnel junction (MTJ) is a spintronic device which has attracted enormous attention because of applications in non-volatile magnetoresistive random-access memories (MRAM) and next-generation magnetic field sensors [Gallagher, 2006]. It is often claimed that since MRAM is based on metallic structures, it will be less susceptible to radiation effects. However, previous studies on MRAMs mainly focus on the sensitivity of CMOS sense and program circuitry. Very little experimental evidence regarding radiation tolerance of MTJs has been published. Determining the radiation tolerance of MTJs, which are the storage elements of MRAMs, is important for investigating their potential application for space and security.

The performance of the MTJ significantly depends on the properties of tunnel barrier, which separates the two adjacent ferromagnetic layers. Previous study on the MTJ with AlO_x barrier shows that the MTJ are not fully radiation hard under intense swift heavy ion bombardments [Conraux, 2003]. Recently, there has been a great interest in using MgO as the tunnel barrier, of which the crystalline nature yields giant TMR ratios due to the interfacial spin-dependent electronic state with Δ_1 symmetry at the Fermi energy [Mathon, 2001]. Since radiation tolerance of MTJs with MgO barrier is unknown, in the present work, we have chosen MgO-based MTJs to conduct the experiment.

In this thesis, we report the gamma and neutron radiation experiments of the MgO-based MTJs under all the three conditions, i.e. pre-, post-, and during exposure to radiation.

1.2 Thesis Organization

This thesis is organized into five chapters:

Chapter 1 introduces the motivation of this work.

In Chapter 2, I'll give an overview of related development in the spintronics as well as a general description of the electrical and magnetic properties of the MTJ. Spin-dependent tunneling mechanism is detailed in this chapter. Important features, such as temperature dependence and bias voltage dependence of tunnel magnetoresistance (TMR) are discussed.

Chapter 3 talks about the radiation mechanisms. The ionization and displacement damages on semiconductor devices are discussed in this chapter. The basic review in radiation tolerance of CMOS devices is discussed. The potential radiation-induced disorders caused by high energy particles in tunnel barrier and magnetic layers are analyzed.

Chapter 4 reports the experimental results in this chapter. For the gamma-radiation experiment, pre- and post-radiation experimental results are detailed. Neutron-radiation experiments of the MgO-based MTJs under all the three conditions, i.e. pre-, post-, and during exposure to radiation are concluded.

Chapter 5 concludes the thesis and also suggests future work to further investigate the project.

2 Magnetic Tunnel Junction

2.1 Spin-valve Structure

The MTJ consists of two ferromagnetic layers separated by an ultrathin insulating layer. The resistance of the MTJ depends on the configuration of the magnetization of the two ferromagnetic layers, which can be switched separately by an external magnetic field. The spin orientation of the bottom ferromagnetic layer could be pinned by another antiferromagnetic layer via exchange bias, while the top ferromagnetic layers can be switched by the external magnetic field. The combination of an exchange bias, pinned layer and a free layer is known as a spin-valve, shown in figure 2.1. The device exhibits high resistance when the two layers are in antiparallel magnetization, while resistance is lower in the parallel configuration.

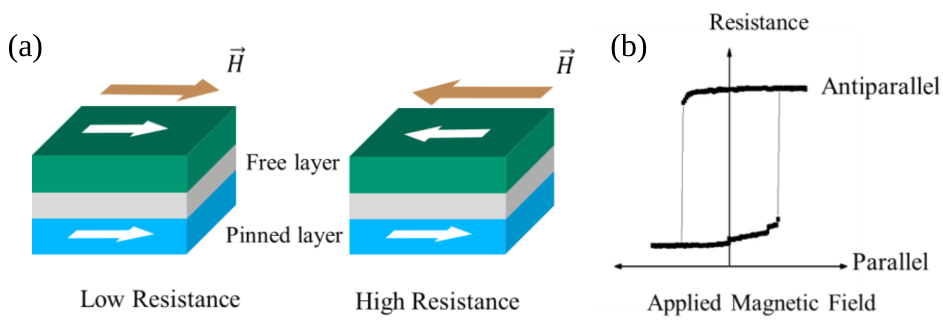

Figure 2.1 A schematic diagram of a spin valve. (a)When the magnetic layers are antiparallel, the resistance is higher than when they are in parallel. (b)The hysterics loop of the MTJ.

Magnetoresistive random access memory (MRAM) is a memory device in which the storage element is a magnetic tunnel junction. This technology recently gained recognition due to its non-volatility, faster write speeds and unlimited endurance. Magnetic orientation in one ferromagnetic layer is pinned while the magnetization of the free layer can be oriented either in the parallel or anti-parallel direction to that of the

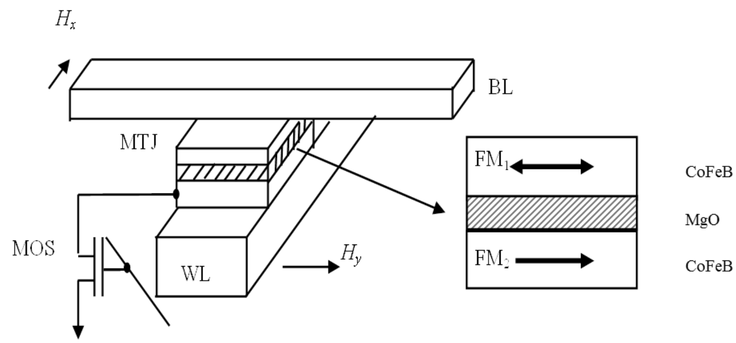

Figure 2.2 A schematic diagram of a magnetoresistive random access memory.

fixed layer. The antiparallel configuration exhibiting high resistance interprets the binary state 1 and the parallel orientation with low resistance interprets 0.

Figure 2.2 shows a schematic diagram of an MRAM. A write pulses passing through the bit line above and word line below are selected to produce the magnetic fields to switch the selected cell. During the “write” operation, the transistor is turned on to bias the MTJ. Reading is realized by measuring and comparing the current passing through the MTJ to a reference current by using a two-stage comparator. Compared with the semiconductor-based memories, radiation tolerance is often claimed as an important asset of MRAMs.

2.2 Magnetoresistance

2.2.1 AMR and GMR

Magnetoresistance is the property of a material to change the resistance when an external magnetic field is applied to it. The first investigations of magnetoresistance in ferromagnetic substances were carried out by W. Thomson in 1857 [Thomson, 1857]. This difference in resistance between the parallel and perpendicular case is called anisotropic magnetoresistance (AMR). AMR is a property of a material in which a dependence of electrical resistance on the angle between the direction of electric current and orientation of magnetic field is observed.

The effect of AMR is attributed to a larger probability of s-d scattering of electrons travelling along the direction of the magnetic field [McGuire, 1975]. Ferromagnetic metals exhibit a normal AMR effect, which the resistivity is at maximum when the direction of current is parallel to the applied magnetic field. In the 1970s, AMR in Iron, Cobalt, and Nickel based materials was exploited when it was found that resistance could change a few percent at room temperature, which promoted the development of AMR sensors for magnetic recording.

Giant Magnetoresistance (GMR) is a large-resistance-change effect which was initially observed in a sandwich Fe/Cr/Fe multilayers [Grünberg, 1989], as shown in figure 2.3. It is currently being utilized in the modern hard drive heads to read the data. GMR is so important that the 2007 Nobel Prize in Physics has been awarded to Grünberg and Fert, the two scientists who discovered this effect. Grünberg's group reported that

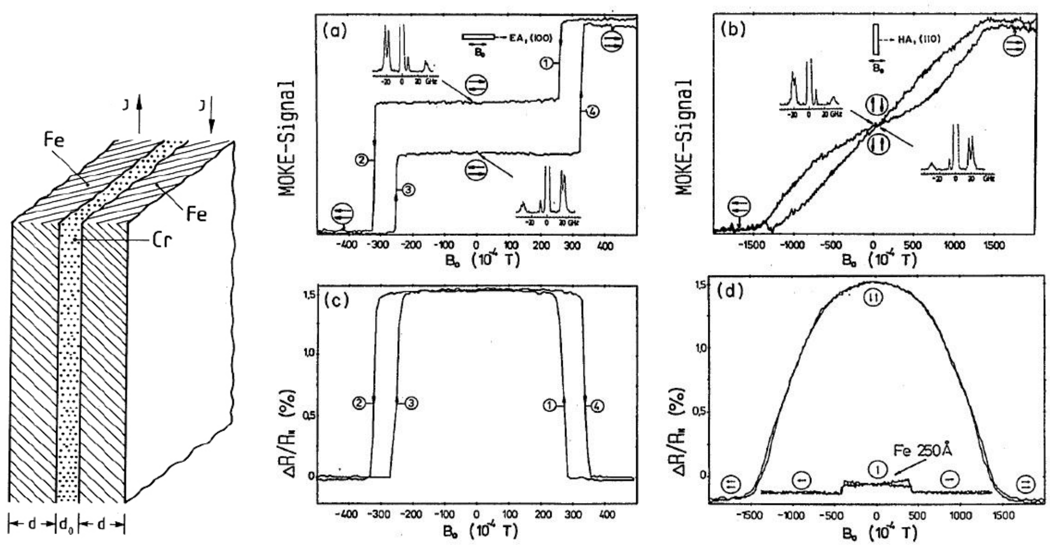

Figure 2.3 GMR effects in a Fe/Cr/Fe multilayer structure, reprinted with permission from [Grünberg, 1988]. Left panel Fe/Cr/Fe shows the sandwich structure. Right panel shows (a) and (b) the hysteresis curves of the device (c) and (d) the resistance as a function of the applied field. In (a) and (c), the field is along easy axis, while in (b) and (d the field is along the hard axis.

resistance was lower when the two FM layers were aligned parallel to each other, and either linear or binary switching could be attained depending on the orientation of the applied field. The relative change of resistance was around 14%, which is shown in figure 2.3. Later, Albert Fert and his group demonstrated that large resistance changes were possible in antiferromagnetically coupled Fe/Cr/Fe trilayers [Baibich, 1988].

GMR is defined as the difference between the resistance of the antiparallel and parallel states normalized by the parallel resistance. The magnetoresistance effect is attributed to the spin-dependent scattering at the interfaces [Camley, 1989].When the ferromagnetic layers are aligned parallel, the resistance is low since only one of the two spin channels are preferentially scattered. When the ferromagnetic layers are antiparallel, however, strong scattering occurs in both spin channels, which causes a larger overall resistance. GMR read heads began to replace those utilizing AMR because the resistance change is much greater than AMR. The large sensitivity of such heads has allowed areal densities in hard drive to reach as high as 0.25 Tbit/in^2 [Wood, 2009].

2.2.2 TMR and Jullière's Model

Tunnel magnetoresistance (TMR) is an extension of spin valve GMR in which the electrons travel with their spins oriented perpendicularly to the layers across a thin insulating tunnel barrier. Jullière made the first successful observation of TMR in MTJs about 1970s, when Co and Fe were used as ferromagnetic materials and Ge as barrier, and a TMR of 14% at low temperature 4.2 K was reported [Jullière, 1975]. After that experiments using different tunnel barriers were reported, e.g. NiO and Gd_2O_3, but only a small TMR value were observed at a low temperature.

It was not until that 1995 MTJ drew great attention when Moodera's group found that using FM/I/FM junctions with an amorphous Al_2O_3 barrier, resulting in a TMR as large as 12% at room temperature [Moodera, 1995], as shown in figure 2.4. Ever since then, MTJs have aroused enormous interest due to their potential applications in spintronic solid state devices, such as high-performance non-volatile MRAMs and the success of magnetoresistive technology for magnetic sensing. TMR ratios as high as 70% were predicted by the TMR equation for MTJs using AlOx barriers [Yuasa, 2002]. Theoretical and experimental work has been focused on increasing the TMR by exploring half-metal layers for MTJs, and studying crystalline tunneling barriers [Mathon, 2001]. Tunnel barriers of crystalline magnesium oxide have been under development since the year 1999. Butler and Mathon predicted that using iron as the ferromagnetic material and MgO as the tunnel barrier, the tunnel magnetoresistance can reach over 1000%. In 2004, Parkin and Yuasa showed a significant TMR in Fe/MgO/Fe junctions that reached over 200% at room temperature. In 2008, MTJs based on the sandwich structure of CoFeB/MgO/CoFeB were observed of TMR of up to 600% at room temperature and more than 1100% at 4.2 K [Ikeda, 2008].

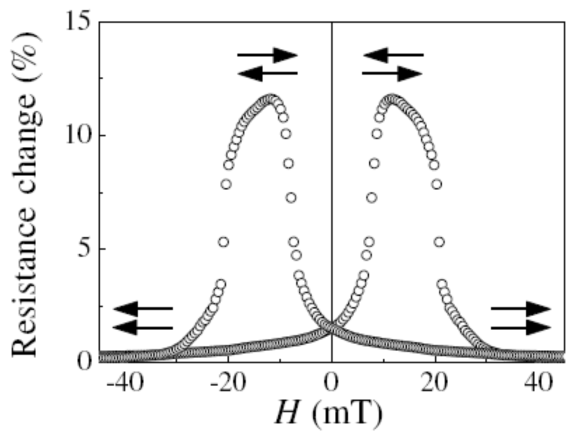

Figure 2.4 The first observation of reproducible large TMR in a $CoFe/Al_2O_3/Co$ MTJ at room temperature, reprinted with permission from [Moodera, 1995].

In non-magnetic materials, the populations of spin-up and -down electrons are equal, which are randomly distributed in an equilibrium state. However, in ferromagnetic materials, electron spins are aligned spontaneously, resulting in unequal numbers of spin-up and -down electrons, as shown in figure 2.5. The alignment of the electron is due to the quantum mechanical exchange interaction. Therefore, in ferromagnetic materials, e.g., Co, Fe, Ni, and their alloys, the band difference between the spin-up and -down electrons is shown on the electronic structures, indicating that the density of states of one spin is

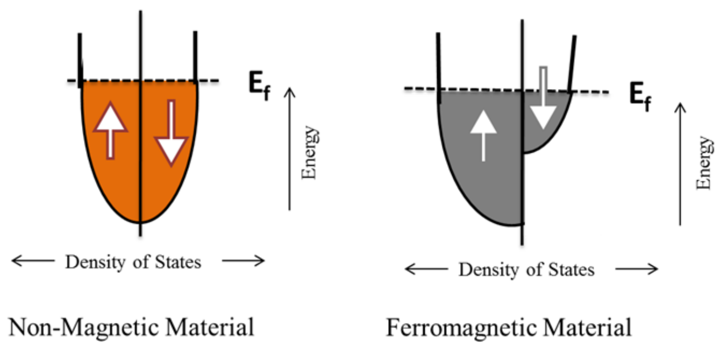

Figure 2.5 A schematic diagram of spin density of states in a non-magnetic material and ferromagnetic material.

greater than the other at the Fermi surface (Figure 2.5).

TMR is defined as the difference between the conductance of parallel and antiparallel magnetizations, normalized by the antiparallel conductance. It can also define as the relative resistance change, which is given by equation 2.1.

$$TMR = \frac{R_{AP} - R_P}{R_P} \tag{2.1}$$

In ferromagnetic materials, due to exchange splitting, Fermi wave vectors for the spin-up and spin-down electrons are different and tunneling probabilities and tunneling current depend on spin consequently.

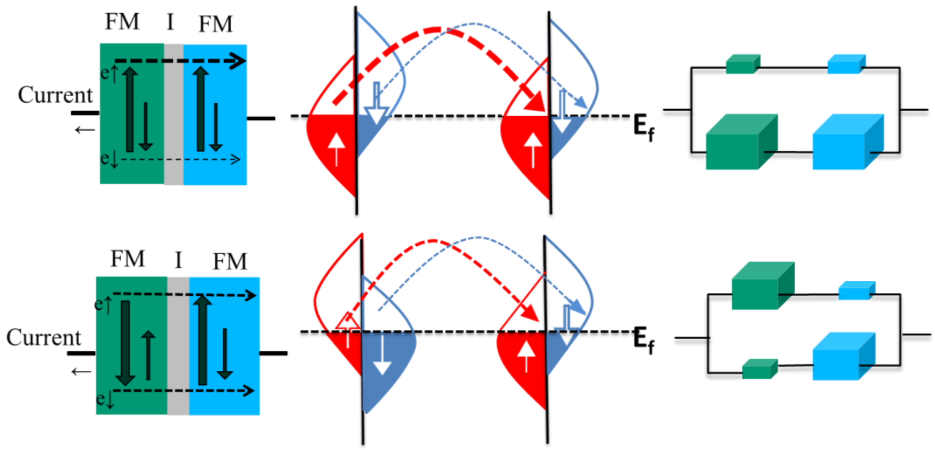

Figure 2.6 Left panel shows An MTJ characterized by parallel or antiparallel magnetization of the left and right ferromagnetic layers. Middle panels shows the schematic representation of transitions between exchange-split spin bands in the ferromagnetic layers. The equivalent circuit diagram is shown on the right panel.

Jullière's model for TMR is based on two assumptions. First, it assumes that spin of electrons is conserved in the tunneling process. The spin-up and spin-down electrons form a two spin channel, where electrons can only tunnel into the empty states of the same spin direction. Figure 2.6 shows the transitions between exchange-split spin bands in the ferromagnetic layers. If the two ferromagnetic layers are in parallel magnetization, the minority spins tunnel to the minority, and the majority spins tunnel to the majority. If the layers are magnetized in antiparallel configuration, the identity of the majority and minority is reversed. The majority-spin electrons of the left ferromagnetic layer tunnel to the minority-spin states in the right ferromagnetic layer and vice versa.

Second, Jullière's model assumes that the spin polarization of the tunneling current is determined by the spin polarization of the total electronic density of states of the ferromagnetic layers at the Fermi energy. Since the number of the electrons tunneling within each spin channel can be determined by the density states of spin up and spin down, the tunneling conductance is weighted by the respective spin density of states. The conductance of parallel and antiparallel configuration can be written in equation 2.2.

$$G_P \propto \rho_L \uparrow \rho_R \uparrow + \rho_L \downarrow \rho_R \downarrow$$
$$G_{AP} \propto \rho_L \uparrow \rho_R \downarrow + \rho_L \downarrow \rho_R \uparrow \tag{2.2}$$

Where $\rho_i\uparrow$ and $\rho_i\downarrow$ (i=left or right) represent the tunneling density of states of spin-up and spin-down electrons, respectively. Introducing the spin polarization, TMR can be expressed in terms of spin polarization, as shown in equation 2.3.

$$Pi = \frac{\rho i \uparrow - \rho i \downarrow}{\rho i \uparrow + \rho i \downarrow} \quad \text{where } i\text{=left, right} \tag{2.3}$$

We also define TMR as the conductance difference in equation 2.4.

$$TMR = \frac{2P_L P_R}{1 - P_L P_R} \tag{2.4}$$

Several factors are important in determining the TMR ratio, including the ferromagnetic materials selection and crystallographic orientation for barrier and ferromagnetic layer. The selection of barrier layer affects TMR significantly. Large TMR values were predicted theoretically for MTJs based on crystalline MgO (001) barrier layers and this prediction was followed by experimental realizations of MTJs utilizing Fe alloy, such as CoFe. CoFeB is frequently used as ferromagnetic electrodes due to its minimum hysteresis. Typically Boron dopant gives CoFe an amorphous structure. Amorphous CoFeB layers appear to crystallize in a bcc structure epitaxial to the MgO surface near the interfaces after annealing treatment. It is clearly shown from equation (3) that higher spin polarization of the ferromagnetic materials give rise to higher TMR. Thus, the half metal ferromagnet aroused interest due to its 100% spin polarization since it is metallic for the majority-spin band but also with an energy gap at the Fermi level for the minority-spin band. In principle, the presence of disorders, such as surface roughness, interface interdiffusion, impurities, and defects such as grain boundaries, stacking faults, and vacancies, will affect the conductance of tunneling significantly.

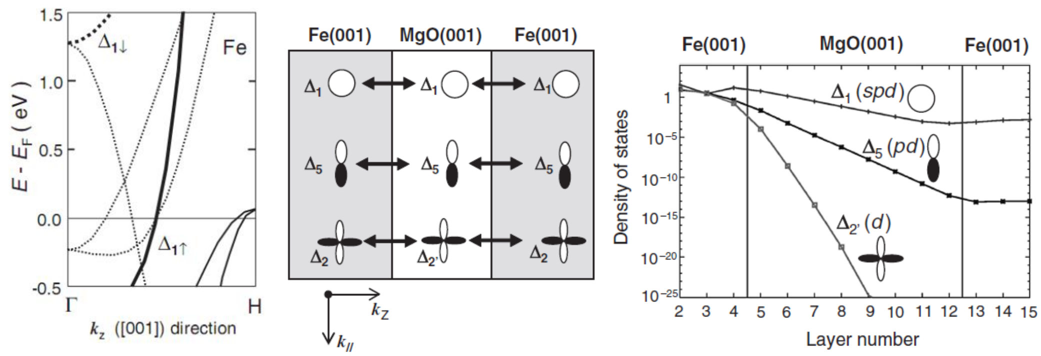

Figure 2.7 Coherent spin dependent tunneling in MgO barrier, reprinted with permission from [Yuasa, 2008]. Left panel shows there is only Δ_1 electrons with one spin polarization at the Fermi energy. Middle panel shows the coherent tunneling of electrons with symmetries. Right panel indicates the Δ_1 electrons have the lowest decay rate in the barrier.

The explanation for a very high MR ratio obtained by Fe/MgO/Fe sandwich structure relies on the coherent spin dependent tunneling in an MTJ with a crystalline tunnel barrier such as MgO(001). For the amorphous tunnel barrier, there is no crystallographic symmetry. With an amorphous insulator, the momentum of a tunneling electron is not conserved, due to scattering within the barrier, and any coherence or symmetry of conducting electrons is destroyed. This tunneling process can be considered as an incoherent tunneling.

Theoretically Δ_1 states in Fe are dominant in tunneling through the MgO(001) barrier for ideal coherent tunneling. In 3d ferromagnetic metals and alloys, symmetric Δ_1 Bloch states usually have a large positive spin polarization at $E_{F,}$ which is desirable for larger TMR. Meanwhile, Bloch states with lower symmetry such as Δ_2 often have a negative spin polarization at E_F.

Right panel in Figure 2.7 shows the partial DOS for the decaying evanescent states in the MgO barrier layer, which is obtained by first-principle calculations. For the calculation, the ferromagnetic layers are assumed at parallel configuration. Of these states, the Δ_1 evanescent states have the longest decay length, which results the slowest decay. Band dispersion of bcc Fe for the [001] direction shows that the full spin-polarization could only be at the Fe Δ_1 band at E_F. Therefore, a large TMR effect in the epitaxially fabricated Fe(001)/MgO(001)/Fe(001) MTJ is expected since Δ_1 electrons dominantly tunnel.

2.3 Important Features

2.3.1 Voltage Dependence of TMR

The current-voltage (I-V) curve of a tunneling device is usually described by the Simmons Theory.

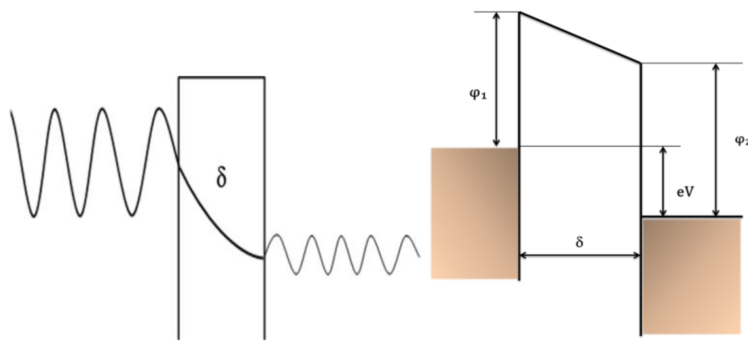

Figure 2.8 Left panel shows a wave-function of a single electron, which is exponentially attenuated within the barrier. Right panel shows the energy diagram of a metal/insulator/metal tunnel junction.

Figure 2.8 shows an energy diagram for a metal/insulator/metal structure. The tunneling current is proportional to the transmission integrated over all energies between the electrodes.

$$I = \frac{2e}{h}\int_{\mu_L}^{\mu_R} T(E)(f_L(E) - f_R(E))dE \tag{2.5}$$

In the equation, f is the Fermi-Dirac distribution function. Therefore, the conductance can be written as

$$G = \frac{I}{V} = \frac{2e^2}{h}T(E_F) \tag{2.6}$$

Simmons theory explains the current density function with bias voltage, which can be expressed as

$$J = \frac{e}{4\pi^2\hbar\delta_z^{\,2}}\left\{\bar{\varphi}\left[\exp(-2\delta_z\frac{\sqrt{2m}}{\hbar}\sqrt{\bar{\varphi}})\right] - \left(\bar{\varphi} + eV\right)\exp\left[-2\delta_z\frac{\sqrt{2m}}{\hbar}\sqrt{\bar{\varphi} + eV}\right]\right\} \tag{2.7}$$

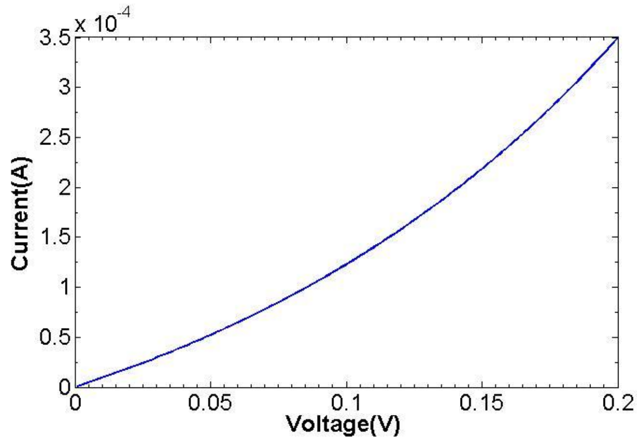

Figure 2.9 The Matlab plot of I-V curve for a tunneling structure FeCo/MgO/FeCo with an effective junction area of 5 μm^2, an effective barrier height 0.9 eV, and a barrier thickness of 12Å.

When the bias voltage applied satisfies $0<V<\bar{\varphi}$, the equation can be modified into an intermediate case as

$$J=\left(\frac{e}{4\pi^2\hbar\delta_z{}^2}\right)\left\{\left(\bar{\varphi}-\frac{eV}{2}\right)\left[\exp(-2\delta_z\frac{\sqrt{2m}}{\hbar})\cdot\sqrt{\bar{\varphi}-\frac{eV}{2}}\right]-\right.$$
$$\left.\left(\bar{\varphi}+\frac{eV}{2}\right)\exp\left[(-2\delta_z\frac{\sqrt{2m}}{\hbar})\sqrt{\bar{\varphi}+\frac{eV}{2}}\right]\right\} \quad (2.8)$$

Figure 2.9 shows The Matlab plot of I-V curve for a tunneling structure FeCo/MgO/FeCo based on the equation 2.8. In the MTJ, both the antiparallel state resistance and parallel state resistance decrease with increasing the voltage, resulting in the overall deduction of TMR, as shown in figure 2.10.

(a)

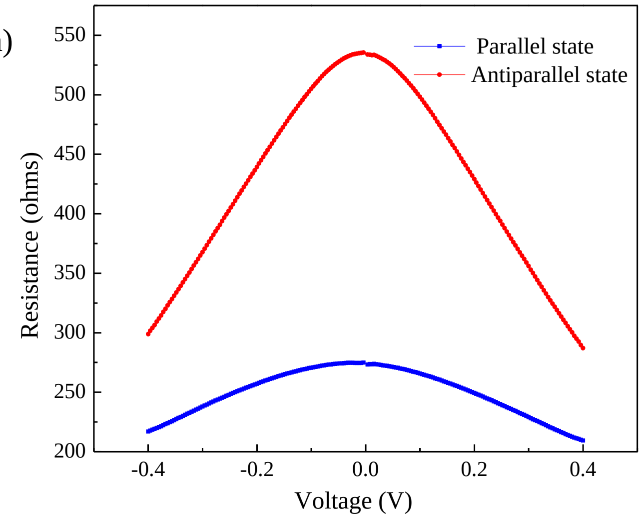

(b)

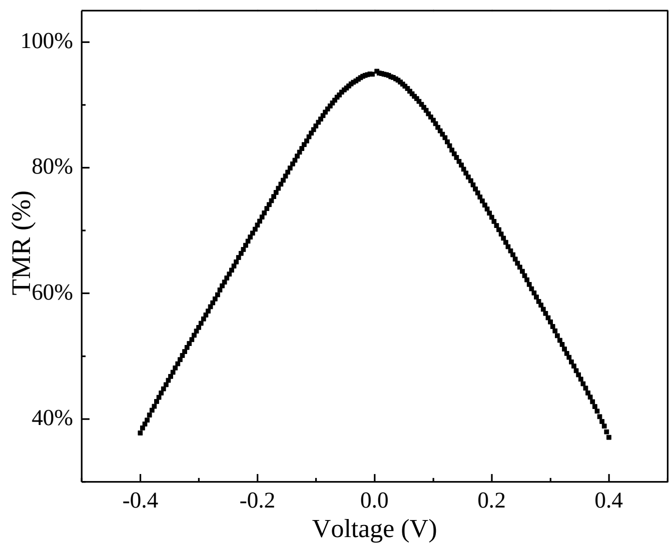

Figure 2.10 (a) Both antiparallel parallel resistances decrease with increasing the voltage. (b) The overall TMR decreases with increasing the voltage.

The most frequently cited explanation for a decreasing TMR with increasing voltage is the emission of magnons at the ferromagnetic-insulator interface [Zhang, 1997]. This model states that a surface magnon is generated when an electron tunnels, which is a coherent excitation of the spins of the ferromagnetic electrodes at the interface with the insulating barrier. As the result, the average surface magnetization is reduced due to the excitation of magnons. The emission of magnon also decreases the surface polarization, which gives rise to the reduction of the TMR. As biased voltage increases, the magnon density of states becomes greater, which results in a stronger effect.

Though the quantitative description is rather complicated than Simmon's model, J-V characterization provides a possible method to analyze the radiation induced changes. Two free parameters d and $\bar{\varphi}$ can be calculated from the experiment data. Studies of radiation effects on Al_2O_3-based MTJs show that, by fitting the data in the J-V relation, potential modifications of the tunnel barrier such as interlayers mixing at the interface or oxygen depletion of the Al_2O_3 layer are limited or spatially localized when the MTJ is exposed in ions ($Ni_{58}^{24+}\ C_{13}^{5+}$) irradiation [Conraux, 2003].

2.3.2 Temperature Dependence

The TMR decreases with increasing temperature in Magnetic Tunnel Junctions. Shang first reported that the temperature dependence of the tunnel resistance for MTJs greatly exceeds that for non-magnetic junctions with nominally identical barriers [Shang, 1998]. For the MTJs with Al_2O_3 barrier, a 15–25% change in resistance was observed for a Co/Al_2O_3/Co junction. The TMR can decrease by as much as 25% or more from 4.2 to 300 K depending on the ferromagnetic materials.

The explanation based on the assumption that the tunneling spin polarization and the interface magnetization followed the same temperature dependence, the Bloch $T^{3/2}$ law,

$$M(T) = M(0)(1-\alpha T^{3/2}) \tag{2.9}$$

Shang provided a satisfactory explanation for the temperature dependence of TMR by fitting parameter α. They also assumed that the tunneling spin polarization decreases with increasing temperature due to spin-wave excitations, as does the surface magnetization.

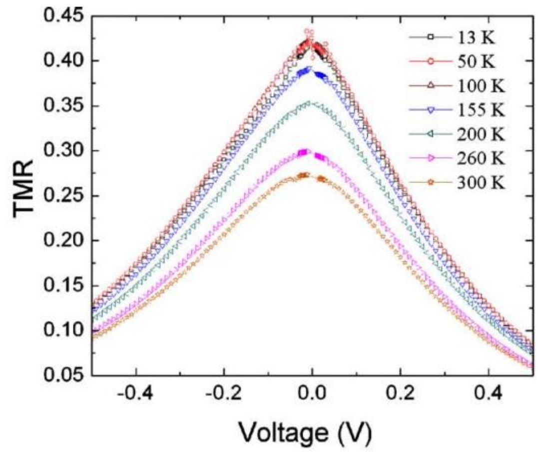

Figure 2.11 The temperature dependence of TMR as a function of biased voltage, reprinted with permission from [Yuan, 2006].

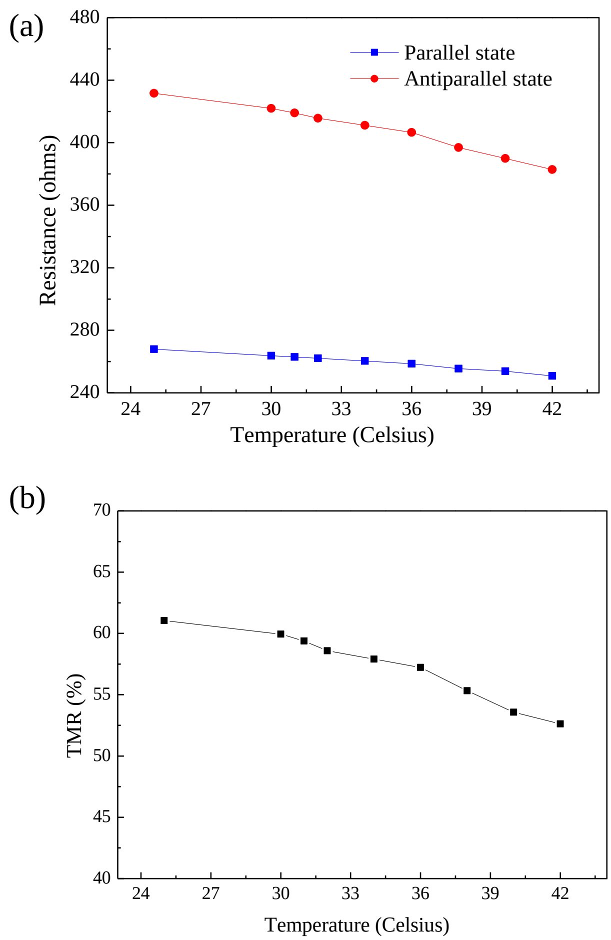

Figure 2.12 (a) Both antiparallel parallel resistances decrease with increasing the temperature. (b) The overall TMR decrease with increasing the temperature.

Another mechanism which results in the reduction of TMR with temperature is explained by the spinflip scattering by magnetic impurities in the barrier layer. When temperature decreases, the increase in R_{AP} occurs more quickly than in R_P, resulting in the increasing TMR ratio. This could be explained by two processes. Due to the contributing of impurities in the barrier, R_{AP} decreases while R_P increases with increasing temperature. On the other hand, the number of electrons contributing to this process increases with increasing temperature. Thermal assist tunneling will result in the reduction of both R_{AP} and R_P with increasing temperature. Due to a combination of these two effects, the increase of resistance in the antiparallel state with decreasing temperature is more than that in the parallel state, resulting in the drop of TMR. In addition, Tsymbal reported that inelastic scattering, in the presence of localized states in the barrier, could contribute to the reduction of TMR [Tsymbal, 2002].

2.4 Conclusion

An overview of related development in the spintronics as well as the tunneling mechanism of magnetic tunnel junction is given in this chapter. The principle for spin dependent transport is explained by Jullière's two-current model, which works quite well for interpreting magnetoresistance data in amorphous MTJ. The temperature dependence and bias voltage dependence of TMR is explained in this chapter.

There are several major challenges for MTJ-based MRAM. First, the thermally activated reversal of the free layer gives rise to error rates. A certain level of energy barrier (this energy barrier to K_BT ratio must be fairly large) has to be maintained for error free non-volatility function. The Second challenge is to integrate TMR with current CMOS processing technology. Third, the demagnetization of the fixed layer results the loss of read-out signal.

Therefore, a new technology, called spin transfer torque (STT) has been claimed to use spin-polarized electrons to directly torque the domains. In STT, spin polarization current is used to flip the spin orientation in the memory devices, which provide better scalability over conventional MRAM using magnetic fields to flip the electrons. Even so, there are major challenges that face spin-transfer based MRAM. Unlike in field-switched MRAM, the MTJs employed in spin-transfer MRAM have to be compatible with relatively high current densities, even if the devices are optimized to minimize current density. Furthermore, high current density sustained in MTJs over time can cause wear-out effects that cause irreversible changes in the resistance of the device.

In conclusion, the spin-intrinsic nature gives magnetic logic circuits different functional principles compared with traditional semiconductor devices, which is claimed as the next generation of radiation-hardened device. The radiation mechanisms will be explained in next chapter.

3 Radiation Effects

3.1 Basic Radiation Mechanisms

Fundamental damage mechanisms in semiconductor materials and devices include displacement damage and ionization damage. The incident particles on a solid lose their energy to ionizing and nonionizing processes as they travel further through the material. Much of this energy loss results in the production of electron-hole pairs and displaced atoms.

Atomic ionization occurs when an electron-hole pair is generated or an electron is removed from the atom. Interaction of high energy photons or charged particles, e.g., protons, electrons, or energetic heavy ions, with the atoms of that material causes the ionization of a target material. In atomic ionization, the ionized electrons can then travel through the material further. Electron-hole pairs can also be generated along the track of secondary electrons emitted via photon-material interactions. Ionization damage is the dominant mechanism of interaction of energetic photons with solid-state materials.

The density of electron-hole pairs generated is proportional to the energy transferred to the target material. Linear energy transfer (LET) expresses the energy transferred to material as an ionizing particle travels through it while stopping power is measure of the energy loss per unit length (dE/dx) of a particle. It is a function of the properties (i.e., mass, energy) of the particle as well as the target material density. The units of LET are commonly expressed as Me·V·cm/g. Total dose effects are phenomena caused by ionization that is defined as the total amount of accumulative radiation received during exposure time. The specified unit of absorbed dose is rad, which denotes the energy absorbed per unit mass of a material.

The bombardment of fast neutrons with solid state materials leads to the displacement of the lattice ions. The primary lattice defects created initially are vacancies and interstitials, as shown in figure 3.1. A vacancy is the absence of an atom from its regular lattice site. If that displaced atom moves into a nearby position that is not usually occupied by an atom, the resulting defect is called an interstitial. A Frenkel pair is known as the combination of a vacancy and an adjacent interstitial. In irradiated silicon, larger local groupings of vacancies may also occur. There are other types of defects can form when vacancies and interstitials are adjacent to impurity atoms, such as the defect-impurity complexes, which is referred to as the E center in irradiated silicon. Incident electrons and photons with energy on the order of 1 MeV produce such point defects in silicon. For energetic ions, only a fraction (<0.1%) of the deposited energy goes into displacements, which results in different types of interactions. In principle, energetic photons cannot directly produce displacements.

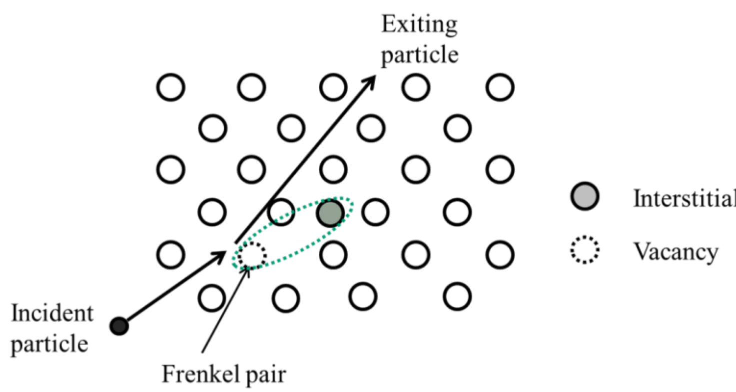

Figure 3.1 The illustration of a Frenkel pair in atomic lattice

Incident neutrons and electrons with energy on the order of 1 MeV produce point defects or isolated defects. A local region of disorder is formed, referred as a defect cluster or disordered region, as the defects may be produced relatively close together. For example, a single incident neutron with energy on the order of 1 MeV gives rise to many defects. A significant amount of energy from that neutron could transfer to a single atom. A disordered region is created as the dislodged primary knock-on atom displaces many other atoms locally. For silicon devices, the defect density produced by a 1 MeV neutron in portions of that local damaged region will be much higher than in electron damage with the equal energy, which is only referred as a subcluster. In general, for displacement damage, incident particles produce a mixture of clustered and isolated defects. Once the defects are formed, they will reorder to form more stable configurations. For example, at room temperature, the vacancy and interstitial in silicon are an unstable defects and are quite mobile. After being introduced, vacancies move through the lattice and form defects that are more stable, e.g., vacancy-impurity complexes. The effectiveness of defects in changing the properties of bulk semiconductor material and devices is determined by the nature of the specific defects and by the time after defect formation at a certain temperature range. Annealing is a common method used for reordering the defect. After annealing, the effectiveness of the defects could be reduced. The reordering of the defect is temperature dependent (thermal annealing) and also dependent on the excess carrier concentration present (injection annealing). Meanwhile, the reordering of defects with time or increased temperature to more stable configurations can result reverse annealing, which could introduce more effective defects. Therefore, the effectiveness of radiation-induced displacement damage depends on the bombardment conditions and also on the time and temperature after irradiation. In general, damage effectiveness depends on many factors, including incident particle type and energy, irradiation conditions, time after irradiation, thermal condition after irradiation, injection level, semiconductor material type, and impurity type and concentration. As a results, the effects of displacement damage lead to the degradation of material and device properties. The radiation-induced disturbance of lattice may give rise to intermediate energy levels in the bandgap. It is the defects, with certain energy levels and states that have an impact on the electrical and other behavior of semiconductor materials and devices. This basic mechanism for the degradation of devices in a radiation environment could be concluded as: 1) incident particles cause the displacement of atoms; 2) new energy levels are generated by the resulting defects; and 3) the intermediate levels could change the material and device electrical, optical and other properties.

3.2 Radiation Effects in CMOS Devices

3.2.1 Photon- and Neutron-induced Effects

CMOS devices are sensitive to photon-induced total dose effects and degradation of the device’s performance typically occurs when dose is greater than 10 krad. Excessive electron-hole pairs and free charges are generated and the buildup of radiation-induced charges trapped in oxide and interface leads to threshold shift and causes the degradation of the devices.

Figure 3.2 shows the fraction of unrecombined holes (charge yield) versus electric field in silicon dioxide [Schwank, 2008]. For all particles, as the electric field strength increases, the probability that a hole will recombine with an electron decreases, and the fraction of unrecombined holes increases. Gamma rays generated by ^{60}Co, which are high energy photons (>100 keV), give rise to the largest amount of unrecombined holes comparing with other radiation sources.

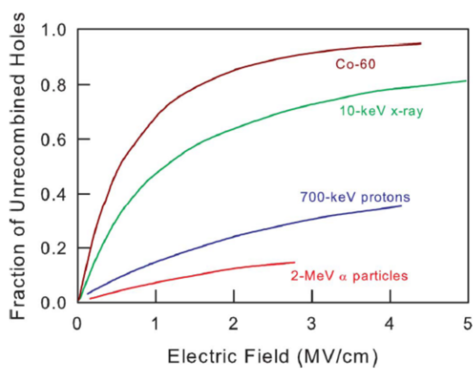

Figure 3.2 The fraction of holes that escape initial recombination for x rays, low energy protons, gamma rays, and alpha particles, reprinted with permission from [Schwank, 2008]

Taking into account the effects of hole yield and electron-hole-pair generation, the total number of holes generated in the oxide that escape initial recombination, N_h is given by

$$N_h = f(E) K_g D t_{ox} \tag{3.1}$$

Where $f(E_{ox})$ is the hole yield as a function of oxide electric field, D is the dose, and t_{ox} is the oxide thickness. In the expression, K_g is a material dependent parameter giving the initial charge pair density per rad. K_g for silicon oxide is 8.1×10^{12} pairs/cm^3. Table 1 shows the typical K_g for different semiconductor materials.

TABLE 1 Typical K_g for different semiconductor materials.

Material	Density (g/cm^3)	Pair density, generated per rad, K_g ($pairs/cm^3$)
GaAs	5.32	7×10^{13}
Silicon	2.328	4×10^{13}
Silicon Dioxide	2.2	8.1×10^{12}

The creation of ionization defects caused by the deposition of energy from ionizing radiation has the physical processes, shown in figure 3.3: 1) the generation of electron-hole pairs, 2) the prompt recombination of a fraction of the generated electron-hole pairs, 3) the transport of free carriers remaining in the oxide. During the process of transport of free carriers, Trapped charge is formed via hole traps in defect precursor. Interface traps are formed due to the presence of hydrogen in the oxide and at the Si–SiO_2 interface.

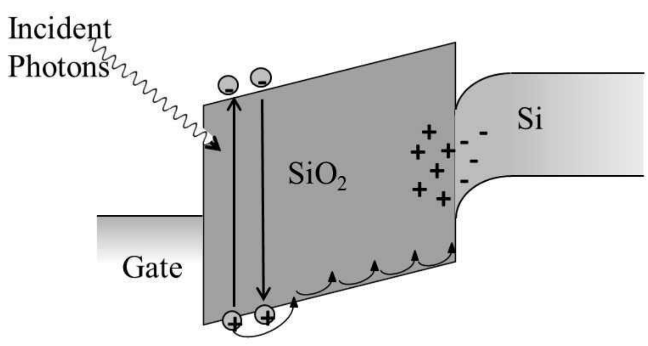

Figure 3.3 Schematic energy band diagram for MOS structure, indicating physical processes underlying radiation response

Figure 3.3 illustrates the basic radiation problem in a MOS transistor. In an N type MOSFET, a conducting channel is formed between the source and drain when an appropriate gate voltage is applied. Electrons flow through the channel so that the device is turned on. Radiation-induced trapped charge in the gate oxide gives rise to a shift in the threshold voltage. For an N type device, a change in the voltage must be applied to turn the device off. If this shift is large enough, even at zero volts applied, the device cannot be turned off.

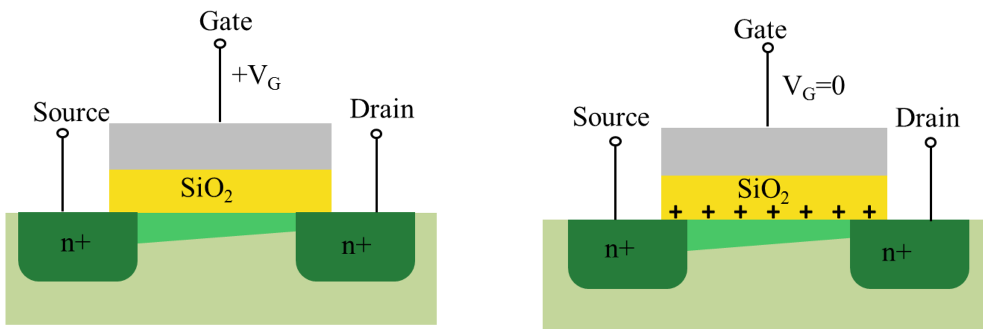

Figure 3.4 Illustration of transistor in normal operation and post irradiation

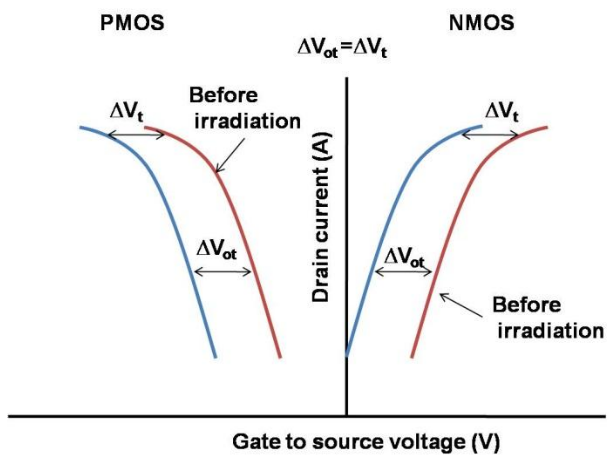

Figure 3.5 Illustration of the effect of fixed oxide trapped charge on n- and p-MOS devices

Fixed charges, which are the charges residing within the oxide very close to the oxide-semiconductor interface, have a significant impact on the CMOS devices. This effect is illustrated in Figure 3.4. The quasi-interface charges will result a negative shift in the DC drain current versus gate-to-source voltage for both n and p-channel MOSFETS, shown in figure 3.5. In n-channel MOSFETs, this shift result a reduction in threshold voltage and an increase in off-state and drive currents. In p-channel MOSFETs, it increases negatively, while off-state and drive currents are reduced. Radiation-induced dc voltage shifts can be calculated using the following equation 3.2:

$$\Delta V_{th} = \Delta V_{ot} + \Delta V_{it} \tag{3.2}$$

ΔV_{ot}, ΔV_{ot} can be determined from the following equation

$$\Delta V_{ot,it} = \frac{-1}{C_{ox} t_{ox}} \int_{o}^{tox} \rho_{ot,it}(x) x dx \tag{3.3}$$

$\rho_{ot,it}(x)$ is the charge distribution of radiation-induced oxide-trapped or interface-trap charge. For present-day gate oxides, the gate oxide thickness is normally very small. Radiation-induced charge buildup rapidly decreases with decreasing oxide thickness. As a result, interface-trap and oxide-trapped charge buildup in gate oxides is often not a concern and total dose effects are dominated by oxide-trapped charge buildup in field oxides. In practice, the radiation-induced charging of the oxide involves several different physical mechanisms, which takes place on very different time scales, with different field dependences and different temperature dependences.

Neutron particles are frequently used for the characterization of the soft error rates (SERs) for semiconductor devices, since this type of error in device output or operation is a result of the ions or neutron radiation striking in a sensitive node in a microelectronic device. While the upset causes a data error, the circuit itself is undamaged; thus, this type of event is called a “soft” error and the rate at which these events occur is called the soft error rate. It has been established that SER in semiconductor devices is induced by three different types of radiation: alpha particles, high energy neutrons and the interaction of thermal neutrons and ^{10}B in devices in devices containing Boron dopants or borophosphosilicate glass (BPSG). Both experimental and theoretical evidence shows that terrestrial neutrons can be a major source of single event upsets (SEUs) in electronics devices. For CMOS technology, Boron is extensively used as a p-type dopant and implants species in silicon and is also used in the BPSG dielectric layers. The boron is added to PSG to reduce its reflow temperature, allowing for improved step coverage and contact reflow at lower temperatures. Boron is composed of two isotopes, ^{11}B (80.1% abundance) and ^{10}B (19.9% abundance), and the thermal neutron capture cross section of

^{10}B is extremely high comparing with other isotopes. When exposed to neutrons, unlike most isotopes, which emit gamma photons after absorbing a neutron, the ^{10}B nucleus breaks apart into excited recoil nucleus and an alpha particle, which are capable of causing SER in memory devices. The SER due to the activation of in BPSG can be mitigated in different ways. The first and most direct method is simply to eliminate BPSG from the process flow. In cases where the unique reflow are needed, the regular BPSG process can be replaced by an enriched process without changing the physical or chemical properties of the film and without the requirement for new processing steps.

3.2.2 Device Scaling and Radiation Hardness

The effects of transistor scaling and geometry on radiation hardness have become an important issue since the total-dose response depends strongly on transistor channel length. Transistors with shorter gate lengths tend to show more negative threshold-voltage shifts than transistors with longer gate lengths during irradiation. During the post-irradiation annealing process, transistors with longer gate lengths tend to show more positive threshold-voltage shifts than transistors with shorter gate lengths. These differences in radiation response, caused by differences in transistor size and geometry, will be important in determining how transistor size and geometry may affect device response in high-dose-rate (e.g., weapon) and low-dose-rate (e.g., space) environments. Therefore, the increased use of commercial deep-submicron technologies in integrated circuits operating in harsh radiation environments is leading to a greater demand for accurate models for radiation effects, e.g., inter- and intra-device leakage effects.

Chip-level measurement in memory devices shows that standby current increases after irradiation of 1 Mrad (Si) [Barnaby, 2009]. As a result, the static power consumption of embedded memory is raised and it also causes a loss of circuit functionality by interfering with proper pre-charging and degrading read stability. The leakage paths created by the radiation-induced defect buildup in isolation oxides mainly contributes to the increased standby current [Brisset, 1996]. These paths include: 1) intra-device leakage between the drain and source of an individual MOSFET and 2) device-to-device leakage between the drains (or sources) of adjacent nMOSFETs or between nMOSFET drainsecource and n-well layers.

Several techniques have been proposed to reduce the effects of radiation-induced charge trapping in the transistor performance. Silicon-on-insulator (SOI) becomes a main-stream commercial technology which also has been developed for radiation-hardened applications. In SOI technology, these techniques can be grouped into two general categories: techniques that reduce the amount of net positive radiation-induced trapped charge and techniques that reduce the effects of radiation-induced trapped charge on transistor performance. One technique to reduce the amount of net radiation-induced trapped charge is to implant silicon in the buried oxide [Ferlet-Cavrois, 2003]. Electron traps are created throughout the silicon implant to buried oxide. As a result, the trapped positive charge will be compensated by the electron traps, which will give rise to the decreasing of the net positive charge in the oxide.

As oxide thickness is decreased, the amount of buildup of radiation-induced charge rapidly decreases. As a result, the importance of radiation-induced charge buildup in gate oxides is rapidly decreasing and the total dose hardness of technologies is dominated by radiation-induced charge buildup in parasitic field oxides and the buried oxides. Two alternate dielectrics, hafnium oxides (HfO_2) and reoxidized nitrided oxides (RNO) have been investigated for replacing silicon dioxide [Miao, 2009]. Hafnium oxides show relatively large hole trapping efficiencies. However, the radiation-induced voltage shifts in these insulators may be negligible for the advanced technologies, which may employ alternate dielectrics. Transistors based on RNO can be fabricated with less oxide-trap charge buildup and there is no measurable interface-trap [Felix, 2004].

Table 3 shows the failure level of total dose effects of some electronic devices. The underlying CMOS circuitry determines that MRAM is with radiation sensitivity. The latest data shows that MRAM devices withstand the total ionizing dose up to 75 krad(Si) with a few read errors. These studies assume that radiation only affects the CMOS circuitry. Thus, the radiation tolerance study of MTJ is unknown and is important for the potential application in MRAM in space and extreme environment.

TABLE 2 Failure level for typical ICs

Technology	Failure level [Krad(Si)]
Linear IC's	2-50
DRAMs	15-50
MRAMs	75-100

3.3 Radiation-induced Disorder in Magnetic Tunnel Junction

Very few studies have addressed the radiation tolerance of spintronic devices. In our study, the radiation-induced disorder in the tunnel junction is investigated by utilizing a resonant tunneling model. Amounts of disorder could be introduced by radiation in the tunneling junctions that affect transport properties.

Radiation-induced disorder in the barrier is of significance in studying the radiation effects on MTJs. Study shows that irradiation of MgO samples with 20 MeV protons leads to the production of anion and cation vacancies [Tench, 1973]. The presence of disorder broadens the conduction and the valence bands of the insulator and creates localized electronic states within the band gap. The formation of localized defect states in the barrier could broaden the bands, which reduces the effective potential barrier for tunneling.

Even more decisive effects could occur if the energy of these states is close to the Fermi energy, which lead to resonance tunneling. Therefore, unlike the propagating states, which is also called bulk states, disorder-assisted tunneling tends to have a resonant nature. A resonant phenomenon of tunneling manifests itself as spikes in the conductance distribution at particular k-points in the Brillouin zone, which is attributed to electrons tunneling via localized states within the band gap of the barrier. The strength of the coupling of the disorder in the barrier with the ferromagnets determines the width of the spikes of the resonance. The reduction of TMR can be understood by a quantitive comparison of spin polarization between a perfect MTJ and a disorder-in-barrier MTJ. Based on the resonant mechanism, the conductance per spin can be written as

$$G = \frac{4e^2}{h} \frac{\Gamma_L \Gamma_R}{(E_F - E_r)^2 + (\Gamma_L + \Gamma_R)^2} \tag{3.4}$$

E_F is the Fermi energy, Er is the energy of the resonant state, Γ_L and Γ_R are the width of the resonance, which can be physically expressed as the rates of leakage of electrons from the impurity state to the left and right ferromagnetic layers. Γ_L and Γ_R are proportional to the density of interface states which can be expressed as equation 3.4, where κ is the decay constant.

$$\begin{aligned} \Gamma_L &\propto \rho_L \exp(-2\kappa x) \\ \Gamma_R &\propto \rho_R \exp[-2\kappa(d - x)] \end{aligned} \tag{3.5}$$

Jullere's model assumes that $|E_F - E_r| \gg \Gamma_L + \Gamma_R$, thus tunneling is off resonance and the conductance in a perfect MTJ can be expressed as $G_P \propto \rho_L \rho_R$.

The position of the resonance could be shifted from the impurity energy Er by δ. Integrating the G with respect to the impurity position and energy, we get

$$G = \frac{4e^2}{h} \frac{\delta e^{-\kappa d}}{2\kappa d} \sqrt{\rho_L \rho_R} \tag{3.6}$$

Thus the spin polarization is reduced compared to an ideal barrier, which could be expressed as

$$Pi = \frac{\sqrt{\rho i}\uparrow - \sqrt{\rho i}\downarrow}{\sqrt{\rho i}\uparrow + \sqrt{\rho i}\downarrow} \tag{3.7}$$

For example, for symmetric ferromagnetic layers, $\rho_i = \rho_L = \rho_R$, if $\rho_L \uparrow / \rho_R \downarrow = 4$, the spin polarization and TMR are calculated in table 3.

TABLE 3 Spin Polarization and TMR in ideal MTJs and disorder-in-barrier MTJs

	Polarization	TMR
Ideal MTJ	60%	112.5%
DIB MTJ	33%	24.9%

(Note: DIB=disorder-in-barrier)

In non-ideal MTJs with amorphous or crystalline barriers, the reduction of spin polarization could be attributed to multiple resonances resulted from the interference of electrons, which are scattered by several localized stated in the barrier. Thus, the situation in MTJs is more complicated than the model explained above. A possible way to observe the predicted strong variation of TMR due to resonant tunneling is to use local characterization techniques such as STM and BEEM. The tunneling spin polarization in MTJs is not only determined by the properties of atomic and electronic structure of barrier, but also depends on the ferromagnets the entire junction including the ferromagnet/insulator interfaces.

In MTJs, interface states are high density of states close to the interface, and they decay away from the interface. The contribution of interface states to the tunneling conductance of perfect MTJs is normally small. The bulk states, which can also be called propagating states, are important for perfect tunnel junctions. It is important to identify the bulk states in the ferromagnetic layers which are coupled to the slowest-decaying state in the barrier, which may dominate tunneling. High energy particles could give rise to the coupling of interface states with the bulk states in tunnel junctions, which results in additional conduction channels. Under these conditions, the electronic structure of the ferromagnet/insulator interfaces may be important to the tunneling current. Due to the coupling of the bulk states and the interface states, a resonant mechanism of tunneling manifests itself as spikes in the conductance distribution at particular k-points in the two-dimensional Brillouin zone. The strength of the coupling through the barrier determines the width of the spikes of the resonance. These resonance phenomena could also be caused by the localized states in the barrier layer. In asymmetric junctions, this increased DOS leads to higher transmission due to tunneling through the interface resonance. A tight-binding model demonstrates that electronic potential and orbital hybridization at the interface essentially control the conductance.

For metallic MTJ structures, slightly rotations of the pinned layer can induce a small and irreversible decrease of the magnetoresistance. The bombardment of high energy particles could introduce defects of the magnetic domains in the magnetic materials and the spin polarization is reduced due to the presence of the defects. Some studies have shown that intense irradiation of ferromagnetic materials with protons reduces the remanence [Gordon, 1963]. Based on the experiment by Conraux on the MTJ with AlO_x barrier, no effect on the magnetics of the MTJ free layer coercivity, interlayer orange-peel coupling, pinned layer exchange bias field was observed upon heavy ions irradiation with fluences up to $10^{13}/cm^2$ [Conraux, 2003]. The study indicated that amorphous or crystalline metallic compounds are known to be pretty insensitive to swift heavy ions, with energies in the range of 10 MeV/A. Hence, the magnetics of the fully metallic exchange biased multilayers are not expected to be altered.

3.4 Conclusion

In summary, basic radiation mechanisms are concluded in this chapter. High energy particles may introduce disorders in the junction, which is described by the resonant tunneling model. Based on the model, the disorder in barrier and the coupling of interfacial states with the bulk states gives rise to the decrease of spin polarization of magnetic tunnel junction, which result the overall the deduction of TMR ratio.

4 Experimental Results

4.1 Device Structure

The standard layer structure is a simple bottom-pinned stack, which consists of the substrate, a buffer layer, a seed layer, an antiferromagnetic layer, a pinned layer, an insulating layer and a free layer. The full structure is substrate/Ru(60Å)/IrMn(110 Å)/CoFeB(60Å)/ MgO(14 Å)/CoFeB(50Å), as shown in figure 4.1.

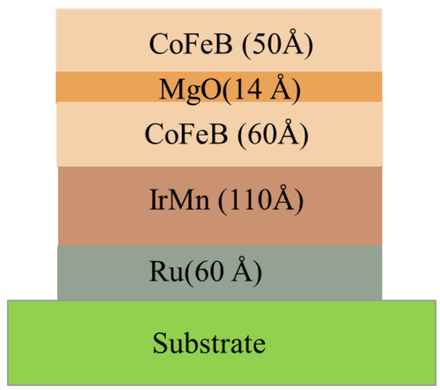

Figure 4.1 The cross section of an MTJ stack

The first layer deposited on the substrate is the seed layer, which is 60 Å of Ruthenium. The role of the seed layer is to improve the texture of the AFM layer. The material used for the antiferromagnetic layer is IrMn. The purpose of this layer is to pin the adjacent magnetic layer via exchange bias to create a spin-valve structure. IrMn is a very good candidate because it is relatively easy to create a well-textured layer. In addition, IrMn is thermally durable due to its high Néel temperature, and its non-corrosive nature prevents long-term degradation.

The tunnel barrier is MgO with (001) crystalline orientation. The uniformity and texture of the tunnel barrier heavily influence TMR values. It is deposited via RF magnetron sputtering and thickness of this barrier is 14 Å.

The ferromagnetic layer is CoFeB, which has composition $Co_{60}Fe_{20}B_{20}$. CoFeB is prepared by sputtering. Boron dopant gives CoFe an amorphous structure, and the use of

CoFeB as the ferromagnetic layer yields high TMR values. Although a high TMR ratio could be measured with the amorphous CoFeB, annealing process is often used. After annealing, the amorphous CoFeB layers crystallize to match the MgO orientation, resulting in highly oriented film in the (001) direction.

4.2 Measurement Techniques

In the experiment, the experimental and control groups of samples were prepared by wire bonding to separate printed circuit boards for the tests. Samples in the experimental groups were exposed to gamma and neutron irradiation respectively, while the control groups received no radiation but were exposed to identical handling and thermal cycles. Then the measurements from the control groups were compared to the experimental groups to determine if the radiation had any effect. The devices were characterized by measuring magnetoresistive hysteresis loops and resistance-voltage curves. The resistance measurement was achieved by a four-point method using Agilent B1500A Semiconductor Device Analyzer. The experimental setup for gamma and neutron radiation tests are indicated in figure 4.2 and 4.4, respectively. For the hysteresis loop (R-H) measurement, the resistance was measured while sweeping a magnetic field along the easy axis at a constant bias voltage. During R-H measurement, the applied magnetic field was limited to 3.8 mT in order to avoid reversal of pinned layer. For the resistance-voltage (R-V) measurement, the resistance was measured while sweeping a bias voltage at a constant magnetic field. Junction death usually occurs with voltage around 1.5 V or higher, therefore, the bias voltage was limited to 0.4 V during the R-V measurement. The temperature dependence of TMR for all the devices was measured to rule out the effects of temperature variations during the experiments. The devices were characterized *in situ* in an environmental chamber.

For the gamma radiation test, the devices in experimental group were characterized before and after exposure to a ^{60}Co gamma ray source. The irradiator is Gammacell 220, which basically consists of an annular source permanently enclosed within a lead shield, a cylindrical drawer, and a drive mechanism to move the drawer along the source center-line. The drawer has a chamber to carry samples to be irradiated from outside the shield to the source. In the *ex situ* measurement, the printed circuit board was positioned in the center of Helmholtz coils, which was powered by the Kepco amplifier. The dose rate was a constant 9.78 rad/minute. The experimental samples initially received a dose of 5.9 Mrad (Si) after which they were again characterized. Irradiation was then continued for a cumulative dose of 10 Mrad, which is significantly greater than the dose for the failure level of CMOS devices. The devices were re-measured electrically and magnetically.

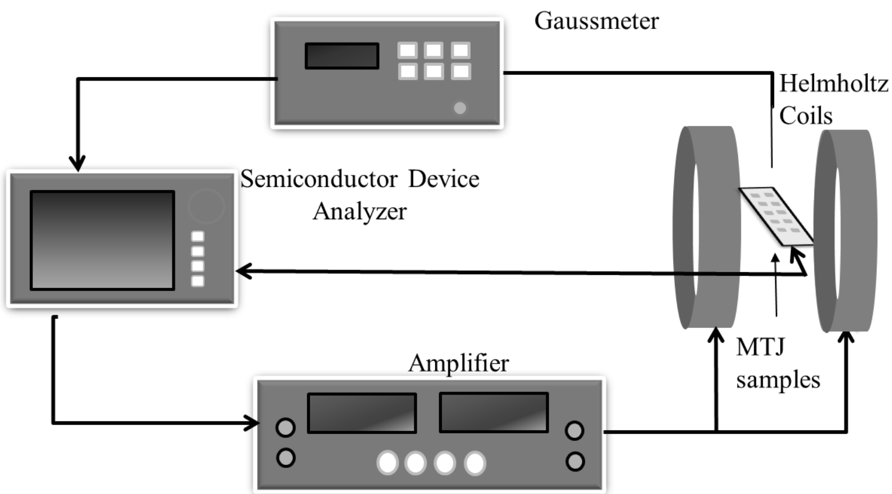

Figure 4.2 The experimental setup for Gamma radiation test

Neutron radiation experiments were conducted at the Oregon State University TRIGA Mk. II research reactor. The experimental group devices were characterized *in situ* in a cadmium-lined in-core irradiation tube (CLICIT). The neutron energies ranged from 0.33 eV to 8.0 MeV, which is indicated in figure 4.3. Cadmium is an important thermal-neutron absorber because one isotope of cadmium, ^{113}Cd, absorbs neutrons with very high probability if the energies are below the cadmium cut-off, which are deemed slow neutrons. The epithermal neutrons, which are intermediate and fast neutrons, are transmitted into the tube. In the experimental setup, the magnetic field was generated by the current passing through the solenoid. A thermocouple was used to monitor the temperature of the samples at the testing. During the irradiation, total epithermal neutron fluence up to $2.9\times10^{15}/cm^2$ was obtained, with the flux at $5\times10^{10}/cm^2sec$.

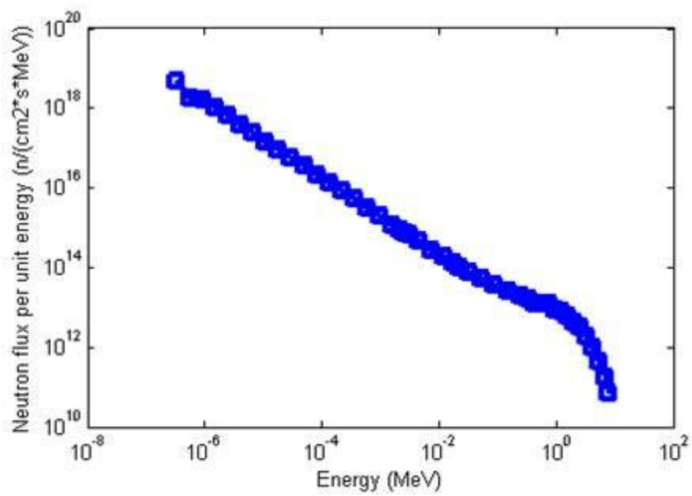

Figure 4.3 The neutron spectrum in CLICIT

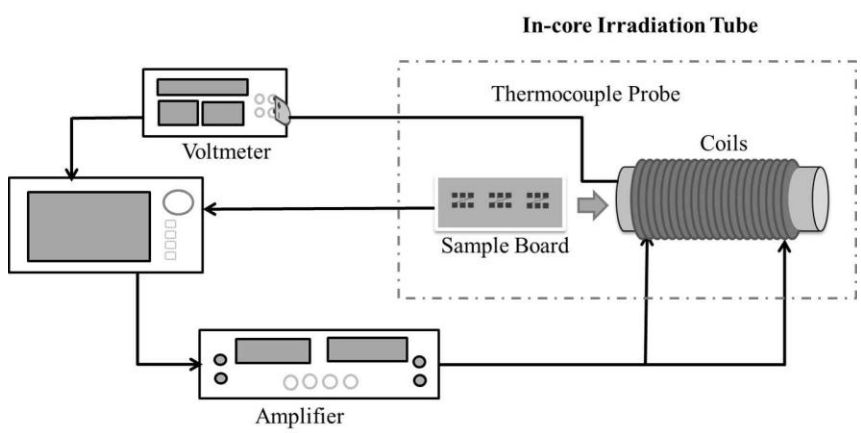

Figure 4.4 The experimental setup for neutron radiation test

4.3 Results and Analysis

Fig. 4.5 shows the characterizations of a single MTJ before and after exposure to the gamma radiation. The hysteresis loop and voltage bias dependence of resistance are shown in Fig. 4.5. TMR could be calculated as the resistance difference between the parallel state and the antiparallel state normalized by the low resistance.

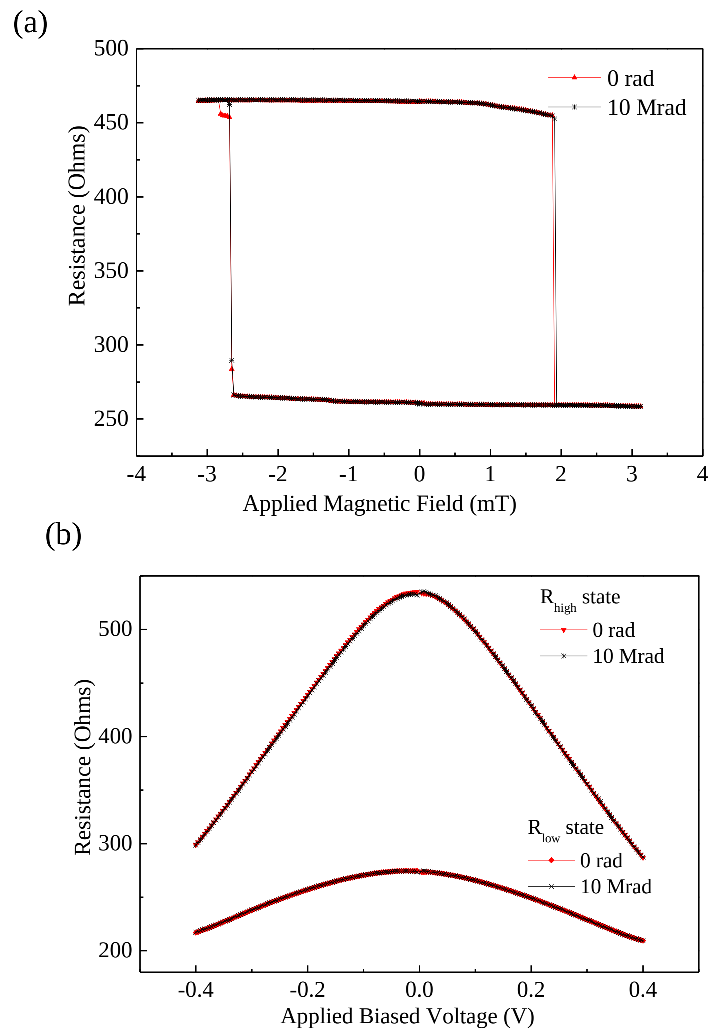

Figure 4.5 Characteristics of a single MTJ before and after exposure to the gamma radiation. (a) The hysteresis loop representing the two resistance states. (b) The voltage bias dependence of the low resistance (R_{low}) state and high resistance (R_{high}) state.

The measured coercive field Hc and TMR of the complete series of control groups and experimental groups are showed in Fig. 4.6 and Fig. 4.7 respectively. The difference in Hc measured before and after exposure to the radiation is much smaller than the device-to-device variation and insignificant compared to the measurement error. That is, the switching field of the junction devices was not perceptibly affected by the neutron fluence of 2.9×10^{15}/cm^2 and accumulated 10 Mrad dose of gamma radiation. After correcting for differences in temperature at the time of testing, the TMR is also found to be unchanged. The control groups, receiving no radiation but being exposed to identical handling, were measured three times at the same time. A Wilcoxon rank-sum test indicates that there is no significant statistical difference between the experimental group data and the control group data.

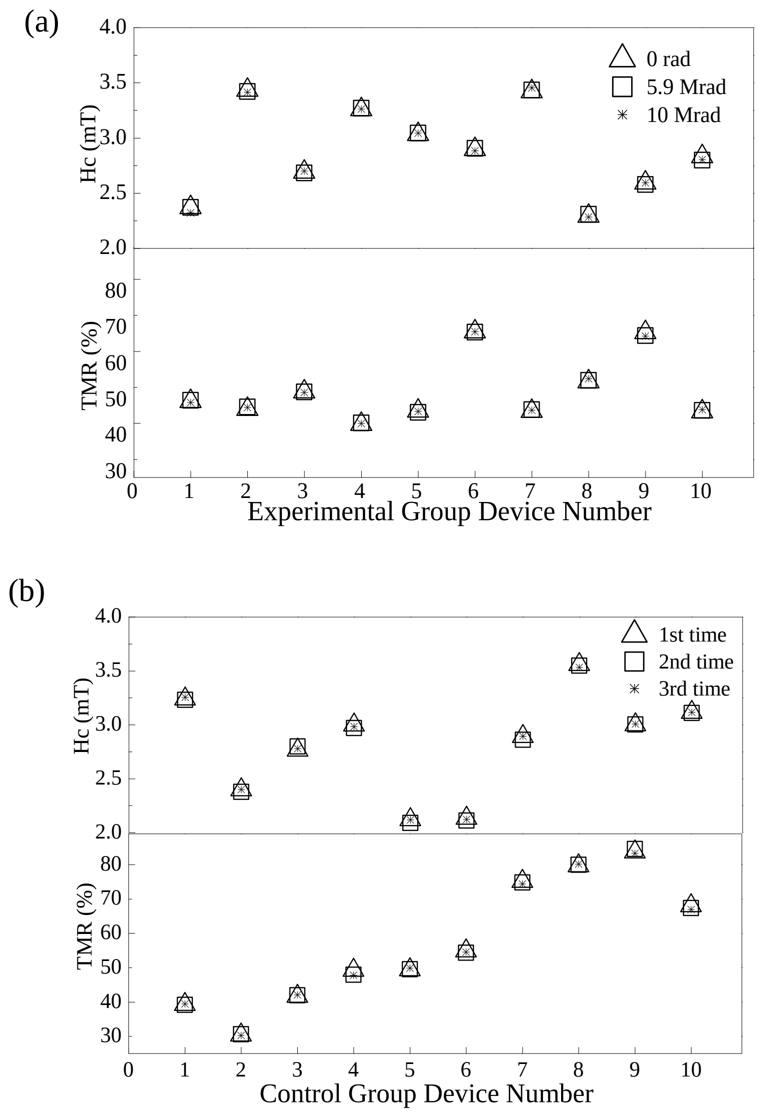

Figure 4.6 Hc and TMR of a series of MTJs before and after exposure to the gamma radiation. (a) Characteristics of the experimental group. (b) Characteristics of the control group, which was not irradiated.

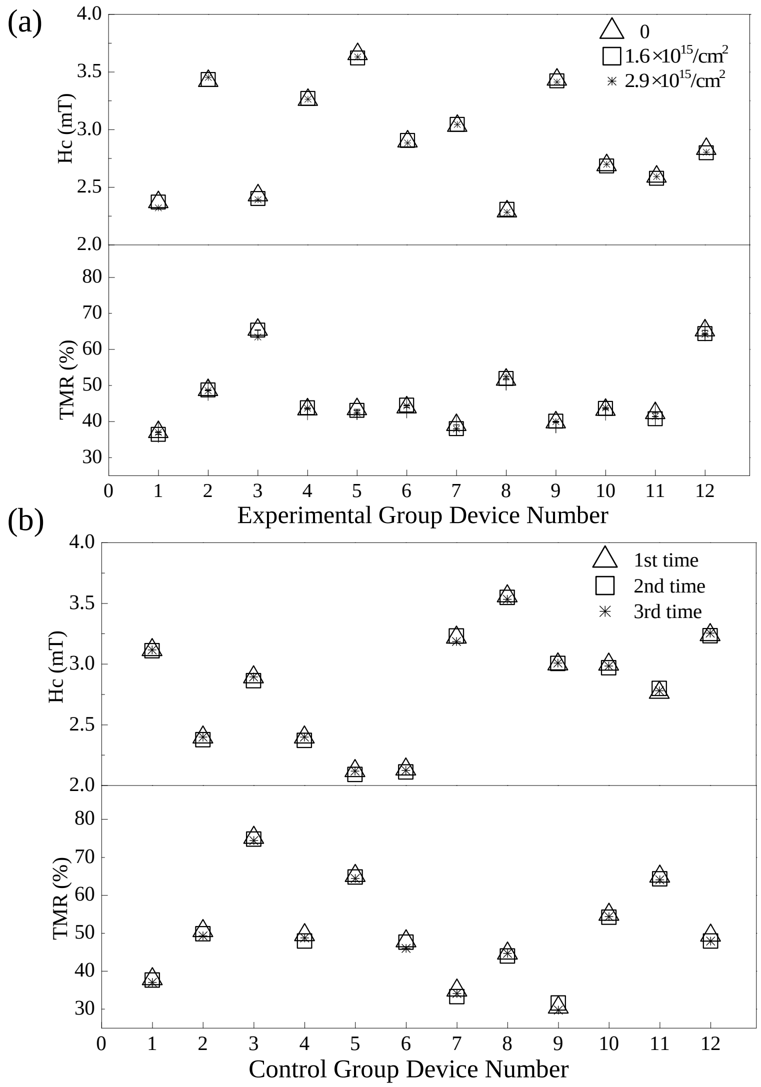

Figure 4.7 Hc and TMR of a series of MTJs before and after exposure to the neutron radiation. (a) Characteristics of the experimental group. (b) Characteristics of the control group, which was not irradiated.

Ionization damage is the dominant mechanism of interaction of energetic photons with CMOS devices. In our experiment, no charge traps were formed after the irradiation. On the other hand, due to the much higher carrier concentration in metal-based MTJs, the ionized carriers have an insignificant effect on the transport properties. Moreover, no effect on the magnetic properties of the MTJs was observed upon radiation. Amorphous or crystalline soft magnetic metals and alloys have structure that is insensitive to epithermal neutron radiation.

5 Conclusion and Future Work

In this work, the gamma and neutron radiation effects on MgO-based MTJs are investigated. Tunneling mechanism and radiation-induced disorders in the MTJs are discussed.

Experimental results show that neither the electrical nor the magnetic properties of MTJs are affected by the radiation. It has been determined that MgO-based MTJs are highly tolerant of gamma radiation of up to dose 10 Mrad. However, previous study reports that particularly in comparison to silicon field-effect transistors which have been shown to degrade with gamma ray exposure even as low as 100 Krad. The MTJs are insensitive to the epithermal neutron fluence of $2.9\times10^{15}/cm^2$, a dose which could form defect centers in silicon dioxide, resulting inter-leakage and intra-leakage in CMOS devices.

In the future, the effect of fast neutron with energy greater than 10 MeV is suggested to be investigated. For neutrons, 10 MeV is often taken to be the lowest energy to which CMOS devices are sensitive. However, due to the device scaling and lower voltage, the lower-energy neutrons can cause SEUs in certain devices and the impact of neutrons below 10 MeV has become increasingly significant for current technologies. Measurement of the fast-neutron-induced device failure is complicated because high-energy neutrons are not widely available. A method is often used to obtain a “white” neutron beam with an energy spectrum similar to the atmospheric neutron spectrum, e.g., the neutron beam at Weapon Neutron Research (WNR) in Los Alamos National Laboratory. At WNR, neutrons with energy ranging from 1-800 MeV are produced in spallation reactions of 800 MeV protons incident on a tungsten target. This beam has been widely used for testing under exposure of high energy neutrons.

On the other hand, irradiation in thermal neutron with energies lower than 0.1 eV is also suggested for CoFeB/MgO/CoFeB structure. CoFeB is possibly susceptible to thermal neutron due to the presence of Boron, since ^{10}B has a large cross section of thermal neutron. The ^{10}B nucleus breaks apart into excited recoil nucleus and an alpha particle after absorbing a neutron, which may possibly give rise to defects in the ferromagnetic layer, resulting spinflip and other effects.

Bibliography

Baibich, M., Broto, J.M., Fert, A., Nguye Van Dau, F., and Petroff, F., "Giant Magnetoresistance of (001)Fe/(001)Cr magnetic superlattice," *Physical Review Letters*, vol.61, pp. 2472-2475, Nov 1988.

Binasch, G., Grünberg, P., Saurenbach, F., and Zinn, W., "Enhanced magnetoresistance in layered magnetic structures with antiferromagnetic interlayer exchange." *Physical Review B*, vol. 39, pp. 4828-2830, Mar 1989.

Camley, R. E., and Barnaś. J., "Theory of giant magnetoresistance effects in magnetic layered structures with antiferromagnetic coupling." *Physical Review Letters*, vol. 63, pp. 664-667, Mar 1989.

Cleaeys, C., and Simoen, E., *Radiation Effects in Advanced Semiconductor Materials and Devices*, New York: Springer, 2002, pp. 12-13.

Conraux, Y., and Nozie`res, J. P., "Effects of swift heavy ion bombardment on magnetic tunnel junction functional properties." *Journal of Applied Physics,* vol.93, pp.7301-7303, May 2003.

Dodd, P.E., "Current and future challenges in radiation effects on CMOS electronics," *IEEE Transaction on Nuclear Science*, vol. 57, pp. 1747 - 1763, Aug 2010.

Dunlop, A., Lesueur, D., Legrand, P., Dammak, H., "Effects induced by high electronic excitations in pure metals: A detailed study in iron," *Nuclear Instruments and Methods in Physics Research Section B: Beam Interactions with Materials and Atoms*, vol. 90, pp. 330-338, May 1994.

Gallagher, W. J., and Parkin, S.P., "Development of the magnetic tunnel junction MRAM at IBM: From first junctions to a 16-Mb MRAM demonstrator chip," *IBM Journal Of Research And Development*, vol. 50, pp. 5-23, Jan 2006.

Gerardin, S. and Paccagnella, A., "Present and future non-volatile memories for space," *IEEE Transaction on Nuclear Science*, vol. 57, pp. 3016 - 3039, Dec 2010.

Gordon, D. I. and Sery, R. S., "Effects of charged particles and neutrons on magnetic materials," *IEEE Transaction on Nuclear Science*, vol. 10, pp. 20-27, Nov 1963.

Heidecker, J., and Allen, G., "Single event latchup (SEL) and total ionizing dose (TID) of a 1 Mbit Magnetoresistive Random Access Memory (MRAM)," *IEEE Radiation Effects Data Workshop (REDW)*, 2010.

Hess, W. N., "Energetic Particles in the Inner Van Allen Belt," *Space Science Reviews*, vol. 1, pp.278-312, Jun 1962.

Hu, Z., Liu, Z., Shao, H., Zhang, Z., Ning, B., Chen, M., Bi, D., and Zou, S., "Comprehensive study on the total dose effects in a 180-nm CMOS technology," *IEEE Transaction on Nuclear Science*, vol. 58, pp.1347-1354, Jun 2011.

Hughes, H. L. and Benedetto, J. M., "Radiation effects and hardening of MOS technology: devices and circuits," *IEEE Transaction on Nuclear Science*, vol. 50, pp. 500-520, Jun 2003.

Ikeda, S., Hayakawa, J., Ashizawa, Y., Lee, Y. M., Miura, K., Hasegawa, H., Tsunoda, M., Matsukura, F., and Ohno, H., "Tunnel magnetoresistance of 604% at 300 K by suppression of Ta diffusion in CoFeB/MgO/CoFeB pseudo-spin-valves annealed at high temperature," *Applied Physics Letters*, vol. 93, pp.082508-082510, Aug 2008.

Mathon, J. and Umerski, A., "Theory of tunneling magnetoresistance of an epitaxial Fe/MgO/Fe(001) junction," *Physical Review B*, vol. 63, pp. 220403-1–220403-4, May 2001.

McGuire, T. "Anisotropic magnetoresistance in ferromagnetic 3d alloys," *IEEE Transactions on Magnetics*, vol. 11, pp.1018-1038, Jul 1975.

Miao, B., Mahapatra, R., Jenkins, R., Silvie, J., Wright, N. G., and Horsfall, A. B., "Radiation induced change in defect density in hfO_2-based MIM capacitors," *IEEE Transaction on Nuclear Science*, vol. 56, pp. 2916-2924. Oct. 2009.

Moodera, J. S., Kinder, Lisa R., Wong, T. M., and Meservey, R., "Large magnetoresistance at room temperature in ferromagnetic thin film tunnel junctions," *Physical Review Letters*, vol. 74, pp. 3273-3276, Apr. 1995.

Pantelides, S. T., Mickish, D. J. , and Kunz, A. B., "Electronic structure and properties of magnesium oxide," *Physical Review B*, vol 10, pp. 5203–5212, Dec 1974.

Parkin, S. S. P., Kaiser, C., Panchula, A. F., Rice, P., Samant, M. G., Yang, S.-H., and Hughes, B., "Giant tunneling magnetoresistance at room temperature with MgO (100) tunnel barriers," *Nature Materials*, vol. 3, pp. 862-867, Oct 2004.

Schwank, J.R., Shaneyfelt, M.R., Fleetwood, D.M., Felix, J.A., Dodd, P.E., Paillet, P., Ferlet-Cavrois, V., “Radiation effects in MOS oxides,” *IEEE Transaction on Nuclear Science*, vol. 55, pp. 1833-1853, Aug 2008.

Shang, C., Nowak, J., Jansen, R., and Moodera, J. S., “Temperature dependence of magnetoresistance and surface magnetization in ferromagnetic tunnel junctions,” *Physical Review B*, vol. 58, pp. R2917-R2920, Aug 1998.

Shen, W. “Ultra-sensitive mgo-based Magnetic Tunnel Junctions for Spintronic Immunoassay.” Ph.D dissertation, Brown University, 2007.

Srour, J.R., “Review of Displacement Damage Effects in Silicon Devices,” *IEEE Transaction on Nuclear Science,* vol. 50, pp. 653-670, Jun 2003.

Thomson, W., “On the electro-dynamic qualities of metals: effects of magnetization on the electric conductivity of nickel and of iron,” *Proceedings of the Royal Society of London*, vol. 8, pp.546-550, June 1857.

Tsymbal, E. Y., Burlakov, V. M., Oleinik, I. I., “Spin injection into amorphous semiconductors,” *Physical Review B,* vol. 66, pp. 0732011-0732014, Aug 2002.

Wolf, S. A., Awschalom, D. D., Buhrman, R. A., Daughton, J. M., von Molnár, S., Roukes, M. L., Chtchelkanova, A. Y. and Treger, D. M., “Spintronics: a spin-based electronics vision for the future,” *Science,* vol. 294, pp. 1488-1495, Nov. 2001.

Wood, R., “Future hard disk drive systems,” *Journal of Magnetism and Magnetic Materials*, vol. 321, pp. 555–561, Mar 2009.

Yuan, L., Liou, S., and Wang, D., "Temperature dependence of magnetoresistance in magnetic tunnel junctions with different free layer structures," *Physical Review B*, vol. 73, pp.134403-1–134403-8, Apr 2006.

Yuasa, S., "Giant Tunneling Magnetoresistance in mgo-based Magnetic Tunnel Junctions," *Journal of the Physical Society of Japan*, vol. 77, pp. 031001-1–031001-13, Mar 2008.

Yuasa, S., Nagahama, T., and Suzuki, Y., "Spin-polarized resonant tunneling in magnetic tunnel junctions," *Science*, vol.297, pp.234-237, Jul 2002.

Yuasa, S., Nagahama, T., Fukushima, A., Suzuki, Y., and Ando, K., "Giant roomtemperature magnetoresistance in single-crystal Fe/MgO/Fe magnetic tunnel junctions," *Nature Materials*, vol. 3, 868-871, Dec 2004.

Zhang, S., Levy, P.M., Marley, A.C., and Parkin, S.S.P., "Quenching of magnetoresistance by hot electrons in magnetic tunnel junctions," *Physical Review Letters*, vol. 79, pp. 3744-3747, Nov 1997.

Žutić, I., Fabian, J., Sarma, S. D., "Spintronics: Fundamentals and applications," *Reviews of Modern Physics*, vol. 76, pp. 323-410, Apr 2004.